MATERIALS CHEMISTRY FRONTIERS

CHINESE CHEMICAL SOCIETY

ROYAL SOCIETY OF CHEMISTRY

RESEARCH ARTICLE

View Article Online
View Journal | View Issue

Cite this: *Mater. Chem. Front.*, 2021, **5**, 4672

Research on metallic chalcogen-functionalized monolayer-puckered V_2CX_2 (X = S, Se, and Te) as promising Li-ion battery anode materials

Chunmei Tang, *[a] Xiaoxu Wang[a] and Shengli Zhang *[b]

Received 17th March 2021,
Accepted 16th April 2021

DOI: 10.1039/d1qm00422k

rsc.li/frontiers-materials

Two-dimensional MXene nanomaterials are promising anode materials for Li-ion batteries (LIBs) due to their excellent conductivity, large surface area, and high Li capability. The chalcogen-terminated monolayer-puckered V_2CX_2 (X = S, Se, and Te) structures are expected to embody remarkable properties for Li storage and diffusion in this paper. The metallic property enables the V_2CX_2 anodes to have a fast electron transport rate in the charge/discharge process. The phonon spectra prove their dynamical stabilities. The adsorption energy and energy diffusion barrier of the Li atom on the V_2CX_2 (X = S, Se, and Te) surface both decrease with increasing atomic number of the terminated element. The monolayer V_2CSe_2 shows higher Li capacity (394.41 mA h g^{-1}), relatively low $E_{barrier}$ (0.21 eV) and a small volume expansion ratio (6.1%) when compared with those of V_2CX_2 (X = O, S, and Te) monolayers, indicating that they should be the most promising LIB anodes. These excellent properties indicate that monolayer chalcogen-terminated V_2CX_2 (X = S, Se, and Te) structures have promising applications as LIB anodes.

1. Introduction

Clean energy is a perpetual topic for environment protection with increasing air pollution brought by the burning of fossil fuels for decades. The high energy density and excellent cycling performance of Li-ion batteries (LIBs) enable them to become the major power supplier for electric vehicles and portable electronics, which extensively depend on clean energy storage devices.[1] The small volume expansion ratio (VER) of the anode and low diffusion energy barrier ($E_{barrier}$) of Li^+ in the anode will promote the excellent cycling performance of LIBs, which can retain the remarkable electrode capacity in the charge and discharge cycle.[2,3]

Numerous two-dimensional (2D) materials, such as graphene, graphdiyne, and transition metal chalcogenides, show promising prospects as LIB anodes.[4–6] Recently, MXenes, as a new family of 2D materials,[7] have shown promising performance as LIB anodes,[8,9] attributed to their high conductivities and large surfaces. The formula for MXene is $M_{n+1}AX_n$ (n = 1, 2 or 3), where M stands for the transition metal (Ti, V, Cr, *etc.*), A comes from group IIIA or IVA (Al, Si, Sn, *etc.*) and X is C or N.[10] There are more than 20 types of MXenes that have been synthesized experimentally and more than 50 types of MXenes that have been predicted by computer simulations.[7,11] The drive for exploring MXenes as LIB anodes is mainly attributed to the high Li capacity and low $E_{barrier}$ of the Li atom, which result in high cycling rate.[12] Importantly, most MXene structures can provide high electrical conductivity.[13] For example, the 2D MXene material Ti_3C_4 monolayer shows a metallic band characteristic and has high capacity as the anode of Na- ion batteries.[14] Such as in the monolayer V_4C_3,[15] the Fermi energy (E_f) of the MXene materials is mainly contributed by the d orbitals of transition metals. The monolayer Mn_2C shows low $E_{barrier}$ (0.05 eV) and high theoretical Li capacity (879 mA h g^{-1}).[16] After 100 charging/discharging cycles, $Nb_4C_3T_x$ has increased specific Li capacity to 380 mA h g^{-1} and exhibited excellent rate capability.[17] The Li capacity of monolayer V_2NS_2 and monolayer Ti_2NS_2 can reach 299.5 mA h g^{-1} and 308.3 mA h g^{-1}, respectively.[18]

Experimentally, MXene structures are always terminated with functional groups –F, –OH or –O on the surface in their synthesis process.[19–22] Bare MXenes are unstable in aqueous solution or open air.[23] Recently, the –OH group can be replaced by a –S (or S^{2-}) group during the heat treatment as known from the XPS analysis experiment.[24] Moreover, it has been theoretically demonstrated that the substitution of –O(–F and –OH) groups on the MXene by the –S group is indeed possible[12] and the S-terminated MXene structures show excellent performance as LIB anodes in previous research.[25–27]

[a] *College of Science, Hohai University, Nanjing, Jiangsu, 210098, P. R. China*
[b] *Key Laboratory of Advanced Display Materials and Devices, and Ministry of Industry and Information Technology, College of Material Science and Engineering, Nanjing University of Science and Technology, Nanjing 210094, P. R. China*

Recent experimental and theoretical investigations have suggested that the energy capacities of MXene structures are strongly dependent on the functional groups.[26,28] The monolayer V_2C, as a new member of the MXenes, has been experimentally synthesized,[29] which is one promising anode for LIBs and has a high theoretical Li capacity of 940 mA h g^{-1} and low $E_{barrier}$ for Li^+.[30] The Li capacity of the V_2CO_2 monolayer was theoretically 376 mA h g^{-1},[31,32] while its experimental Li capacity was 260 mA h g^{-1} under the high charge/discharge rate.[9] Therefore, more research is needed to explore the monolayer V_2C with better electrochemical performance.

The S-terminated V_2C monolayer has shown excellent performance as the LIB anode or when applied in Li–S batteries in previous research.[33–35] In the periodic table of elements, since S, Se, Te and O are in the same column, the chalcogen-terminated puckered V_2CX_2 (X = S, Se, and Te) monolayers are expected to embody remarkable performance when used as the LIB anodes. $Ti_{n+1}C_n$ (n = 1, and 2) MXenes terminated with selenium and tellurium have been synthetized experimentally in 2020.[36] Sulfidation can replace oxygen with sulfur element.[37] Until now, the Se- and Te-terminated V_2C monolayers have not been reported. We will systematically investigate the possibilities of chalcogen-terminated monolayer-puckered V_2CX_2 (X = S, Se, and Te) and explore their application as LIB anodes in this paper. Our calculated results reveal that the monolayer V_2CSe_2 shows a higher Li capacity than V_2CX_2 (X = O, S, and Te) monolayer and the reduced $E_{barrier}$ for the Li^+ ion compared with that of the monolayer V_2CO_2.

2. Computational methods

The Vienna *ab initio* simulation package (VASP) software, in which the electron-ion interaction is described by the projector augmented wave (PAW) method,[38,39] is used to perform all the first-principles calculations in this paper.[40] Based on the generalized gradient approximation (GGA), the Perdew–Burke–Ernzerhof (PBE) functional is used to treat the electron correlation interaction.[41,42] The cutoff energy of the plane wave is set to be 600 eV. In order to avoid the interlayer interaction caused by the period boundary condition, in the direction perpendicular to the surface, a vacuum layer of 30 Å is applied. In the optimization process, the Brillouin zone is sampled by the 4 × 4 k-point for the 3 × 3 super cell with the convergence criteria of 0.01 eV $Å^{-1}$ for the force and 10^{-6} eV for the energy. The van der Waals (vdW) interaction is taken into consideration by using the Grimme DFT-D2 dispersion correction method.[43] The phonon spectra are calculated by using the Phonopy code[44] interfaced with the VASP software. By using both the climbing image nudged elastic band (CI-NEB) and nudged elastic band (NEB) method,[45,46] the diffusion of the Li^+ along many pathways on monolayer V_2CX_2 (X = S, Se, and Te) are considered. Additionally, the *ab initio* molecular dynamics (AIMD) simulations are carried out to examine the thermal stability of the 3 × 3 super cell for Li atom embedded monolayer V_2CX_2 (X = S, Se, and Te) at 300 K. The AIMD method is based on the finite temperature of the local density approximation (with free energy as a variable) and diagonal to each MD step with effective matrix solution and effective Pulay mixed solution of instantaneous electronic ground state. The NVT ensemble is carried out to balance the system at 300 K for 5 ps.[47–49]

The monolayer V_2C is firstly calculated to examine the computational method used here. The calculated lattice constant and the V–C bond length for the unit cell are 2.90 Å and 1.99 Å, respectively, which are consistent with the 2.91 Å and 2.00 Å in the previous research.[50] Thus, the computation method used in this paper is reliable.

3. Results and discussion

3.1 The structures and stabilities of the V_2CX_2 monolayer

The structure of the monolayer V_2CX_2 (X = Se and Te) is the same as that of monolayer V_2CS_2, in which the S atom is replaced by Se and Te atoms. The optimized lattice constants of the unit cell for three monolayer structures (V_2CS_2, V_2CSe_2 and V_2CTe_2) are 3.05 Å, 3.12 Å and 3.24 Å, respectively, which are larger than those of 2.91 Å[50] and 2.90 Å[51] for V_2C and V_2CO_2 monolayers. The geometric structures of monolayer V_2CX_2 (X = S, Se, and Te) have up-to-down five X, V, C, V, and X layers, and the two layers of atoms above the C layer are symmetric to those below the C layer, as shown in Fig. 1(a). The band structures of monolayer V_2CX_2 (X = S, Se, and Te) plotted in Fig. 1(b–d) reveal their metallic characteristics and the ultrafast electrical conductivity, which are critical to the LIB anode materials and similar to the case of monolayer $Ti_3C_2S_2$.[26] In

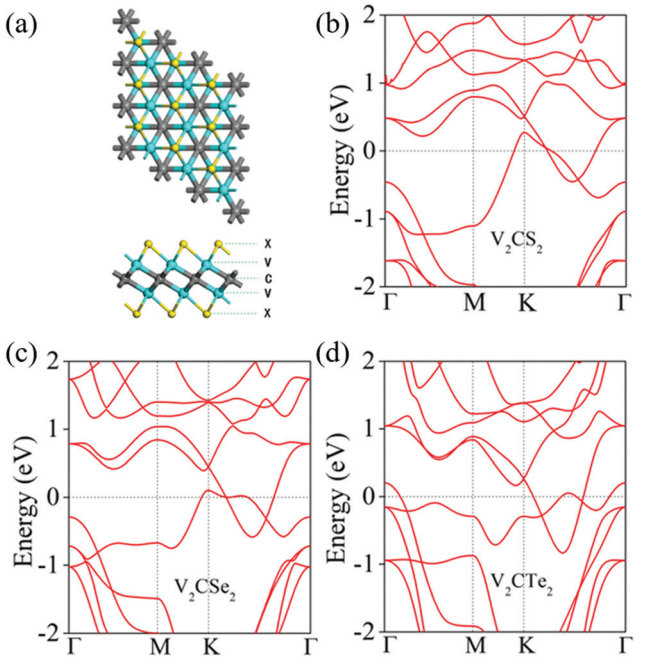

Fig. 1 (a) Top view and side view of chalcogen-functionalized monolayer V_2CX_2 (X = S, Se, and Te). Electronic band structures of (b) monolayer V_2CS_2, (c) monolayer V_2CSe_2 and (d) monolayer V_2CTe_2. The yellow, blue and gray balls represent chalcogen, V, and C atoms.

order to judge whether monolayer V_2C can form stable new structure of V_2CX_2, the formation energy (E_f) is calculated as follows:[34]

$$E_f(X) = 2E(X) + E(V_2C) - E(V_2CX_2) \quad (1)$$

where $E(X)$ refers to the total energy per atom of the S8 molecule (when X = S), Se8 molecule (when X = Se) and metal Te (when X = Te), respectively. The $E(V_2C)$ and $E(V_2CX_2)$ are the total energies of V_2C and V_2CX_2, respectively. The calculated E_f of monolayer V_2CS_2 is 5.09 eV, which is in agreement with the previous research.[34] The E_f are 4.80 eV and 3.25 eV for X = Se and X = Te, respectively. The positive values mean that the formation process of the V_2CX_2 monolayer is exothermic and the phase of the V_2CX_2 monolayer is stable against the separation for all X.

In order to further check the stabilities of monolayer V_2CX_2 (X = S, Se, and Te), the phonon dispersion calculation is performed. The dynamical stability of monolayer V_2CX_2 (X = S, Se, and Te) is obviously verified by the none imaginary frequency in their phonon spectra as shown in Fig. 2(a–c). It can be noticed that, in the phonon spectra of monolayer V_2CS_2, three acoustic branches and twelve optical branches are observed, which are the same as those in the previous research.[35] In the vicinity of the Γ point, there is linear dispersion of two in-plane acoustic branches and a quadratic out-of-plane acoustic branch, which is consistent with that of multilayer materials.[26,52] Thus, these structures should be all dynamically stable. In addition, the thermal stabilities of them are checked by the AIMD simulation. The free energy of V_2CX_2 fluctuates around a constant value during 5 ps of total time at a temperature of 300 K. The time step is 1 fs, as presented in Fig. 2(d–f). The intact structure without any apparent distortion indicates that monolayer V_2CX_2 is thermally stable at room temperature. It should be noticed that the free energy curve of monolayer V_2CS_2 is consistent with that in the previous research.[35]

The mechanical properties are further calculated to check the mechanical stability of the monolayer-puckered V_2CX_2 (X = S, Se, and Te). The four independent elastic constants, C_{11}, C_{12}, C_{22}, and C_{44}, are calculated and presented in Table 1. Clearly, they comply within the Born criteria[53,54] that C_{11}, C_{22}, C_{44}, and $C_{11}C_{22} - C_{12}^2$ should be all positive, implying that V_2CX_2 (X = S, Se, and Te) monolayer has feasible strength to store numerous Li atoms. According to the calculated elastic constant,[55,56] the Young's modulus Y and Poisson' ratio ν along the x and y directions are calculated as follows:[57]

$$Y_x = (C_{11}C_{22} - C_{12}^2)/C_{22} \quad (2)$$

$$Y_y = (C_{11}C_{22} - C_{12}^2)/C_{11} \quad (3)$$

$$\nu_x = C_{12}/C_{22} \quad (4)$$

$$\nu_y = C_{12}/C_{11} \quad (5)$$

The calculated Y_x and Y_y are equal for these 2D monolayer materials, which are 237.45 N m^{-1} for V_2CS_2, 209.62 N m^{-1} for V_2CSe_2 and 132.53 N m^{-1} for V_2CTe_2, respectively. Obviously, the Young's modulus Y of the V_2CX_2 (X = S, Se, and Te) monolayer is greater than those of some other 2D materials, such as monolayer WS_2 (106.4 N m^{-1}), indicating that monolayer-puckered V_2CX_2 (X = S, Se, and Te) has better mechanical strength. The decreased Y of monolayer V_2CX_2 means that the flexibility will increase with the larger mass of X. The calculated ν_x and ν_y for monolayer V_2CX_2 (X = S, Se, and Te) are 0.16, 0.23, and 0.45 respectively.

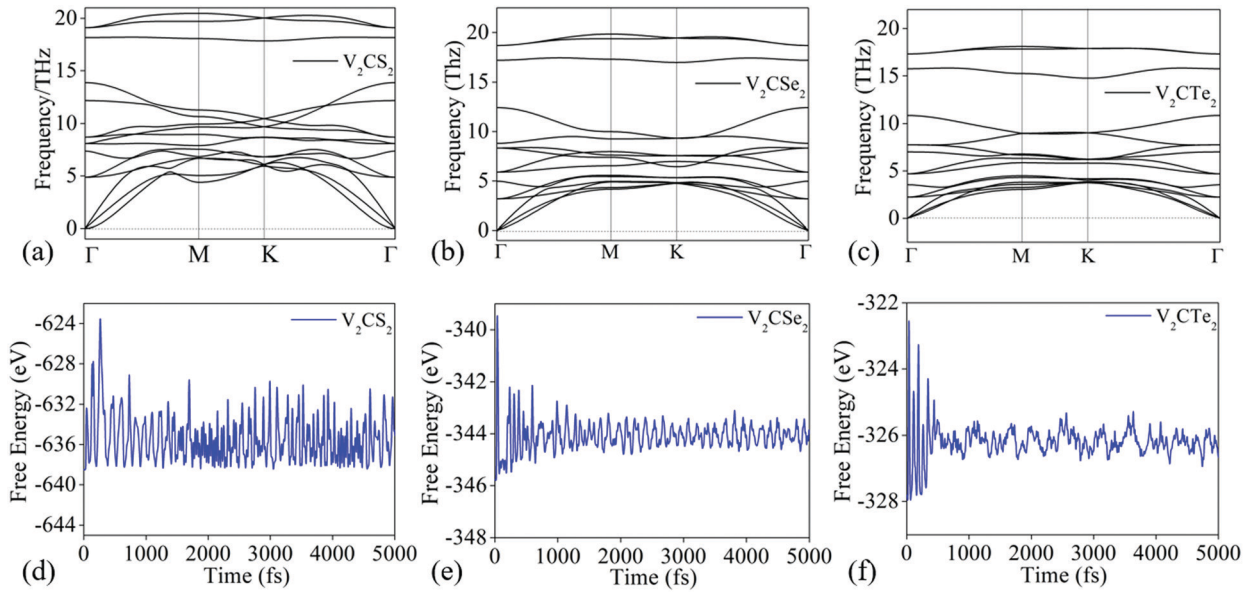

Fig. 2 The calculated phonon band structures of the unit cells of the monolayers (a) V_2CS_2, (b) V_2CSe_2 and (c) V_2CTe_2. The free energy variations of (d) monolayer V_2CS_2, (e) monolayer V_2CSe_2 and (f) monolayer V_2CTe_2 within 5 ps during the AIMD simulation at 300 K.

Table 1 The C11, C12, C22 and C44, Y_x,Y_y, v_x, and v_y of the monolayer V_2CX_2 (X = S, Se, and Te)

	C_{11} (N m^{-1})	C_{12} (N m^{-1})	C_{22} (N m^{-1})	C_{44} (N m^{-1})	Y_x (N m^{-1})	Y_y (N m^{-1})	v_x	v_y
V_2CS_2	243.67	38.94	243.67	102.36	237.45	237.45	0.16	0.16
V_2CSe_2	220.84	49.78	220.84	85.53	209.62	209.62	0.23	0.23
V_2CTe_2	166.70	75.47	166.70	45.61	132.53	132.53	0.45	0.45

3.2 The adsorption and diffusion of the Li atom on monolayer V_2CX_2

Based on the time-cost consideration, the 3 × 3 super cell of monolayer V_2CX_2 (X = S, Se, and Te) is used to study the Li adsorption behavior. As shown in Fig. 5(a), there are three different sites, that is, upon the V atom of the lower layer (site A), upon the C atom (site B), and upon the X atom (site C). The average adsorption energy (E_{ad}) of the Li atom at the above three different sites on monolayer V_2CX_2 is defined in the following:[30]

$$E_{ad} = E_{Li} + E_{V_2CX_2} - E_{V_2CX_2+Li} \quad (6)$$

We take E_{Li} as the energy of bcc-Li. If the E_{ad} is larger than 0 eV, the adsorption strength should be ideal. The strong binding strength between the Li atom and monolayer V_2CX_2 can be reflected by the large positive E_{ad}. Table 2 shows the E_{ad} of one Li atom on the chalcogen-terminated monolayer V_2C. It is found from the E_{ad} that site A should be the most stable. Moreover, the calculated E_{ad}s at site A, B and C decrease with the increased atomic number of chalcogen elements. The Bader charges[58] are calculated to explore the adsorption properties and are shown in Table 3. Obviously, the electron transfer between Li and monolayer V_2CX_2 decreases with the increased electronic layers of chalcogen elements. The three functional groups have little effect on the electron transfer between V and C. It can be known from the table that the heavier chalcogen element has less charge transfer. The difference charge densities are defined in the following:[59]

$$\Delta\rho = \rho(V_2CX_2 + Li) - \rho(V_2CX_2) - \rho(Li) \quad (7)$$

where $\rho(V_2CX_2 + Li)$, $\rho(V_2CX_2)$, and $\rho(Li)$ represent the charge densities of one Li-adsorbed V_2CX_2, pristine V_2CX_2 and one Li atom, respectively.

As shown in Fig. 4, the charge transfer mainly happens between Li and chalcogen atoms. Moreover, Li on the monolayer V_2CX_2 transfers more charge than that from the Li atom to monolayer V_2C (0.80 *e*),[30] which explores the stronger adsorption strength for the Li on the monolayer V_2CX_2 than that on the monolayer V_2C. This can be in good agreement with the larger E_{ad} on monolayer V_2CX_2 than that on monolayer V_2C (0.16 eV).[30] Thus, the heavier chalcogen element can obviously increase the binding strength between Li and the V_2C monolayer. Obviously, it is known from Table 3 that the Li atom on site C loses most electrons. We further investigate the PDOS of one Li atom-adsorbed monolayer V_2CS_2. As shown in Fig. 3. The E_f is at 0 eV. The apparent overlapping of the PDOS of V(d), C(p), and X(p) indicates the strong hybridization among them. The overlapping between the PDOS of the Li atom and monolayer V_2CX_2 indicates the hybridization interaction between them. The PDOS around E_f mainly consists of *V*(d) orbitals, which is the same as that of monolayer V_2CO_2.[31] The area between the PDOS and the energy axis is increasing with the increased electronic layers of chalcogen elements, which is consistent with the Bader charge analysis.[58]

Table 2 The E_{ad} of single Li adsorbed on three different sites on the monolayer V_2CX_2 (X = S, Se, and Te)

E_{ad} (eV)	V_2CS_2	V_2CSe_2	V_2CTe_2
A	1.48	0.94	0.27
B	1.35	0.82	0.19
C	0.66	0.16	−0.45

Table 3 The Bader charges of Li(Q_{Li}), C(Q_C), and V(Q_V) and X (Q_X) in the monolayer V_2CX_2 (X = S, Se, and Te)

	Li site	Q_{Li}	Q_C	Q_V	Q_X
V_2CS_2Li	A	0.892	−1.461	1.285	−0.604
	B	0.901	−1.461	1.285	−0.605
	C	0.927	−1.460	1.282	−0.604
V_2CSe_2Li	A	0.888	−1.504	1.209	−0.506
	B	0.898	−1.506	1.207	−0.504
	C	0.921	−1.505	1.207	−0.506
V_2CTe_2Li	A	0.882	−1.549	1.110	−0.385
	B	0.889	−1.549	1.110	−0.395
	C	0.911	−1.550	1.108	−0.383

To explore the promising properties of monolayer V_2CX_2 as high-rate LIB anode materials, the $E_{barrier}$ along diffusion paths has been investigated for one Li^+ on the monolayer V_2CX_2 by both the CI-NEB and NEB methods.[45] The $E_{barrier}$ is calculated in the following:[60]

$$E_{barrier} = E_{TS} - E_{SS} \quad (8)$$

Here, E_{TS} and E_{SS} are the total energies of the transitional state (TS) and the most stable state (SS) of the Li adsorbed membrane, respectively. We only consider the diffusion path between two neighboring most stable A sites (A → A). The Li atom will go past site B when travelling from site A to another nearest site A (A → B → A) according to the CI-NEB method. The Li atom will shift through site B when travelling from site A to another nearest site A, which is similar to the previous research of monolayer $Ti_3C_2S_2$[26] and monolayer V_2CS_2.[33] As shown in Fig. 5(c), the calculated $E_{barrier}$ values along the A → B diffusion path for V_2CS_2, V_2CSe_2 and V_2CTe_2 monolayers are 0.23 eV, 0.21 eV and 0.19 eV *via* the NEB method, respectively. We can note that the $E_{barrier}$ for the Li atom along the A → A diffusion path is equal to that along the A → B → A path, which are both 0.23 eV based on the CI-NEB method and can indicate the freedom of Li atoms diffusing on the V_2CS_2 substrate. This result is consistent with the previous research of monolayer V_2CS_2 (0.22 eV).[33] Clearly, with the increased electronic layers of chalcogen elements, the $E_{barrier}$ is decreasing continuously. In addition, the $E_{barrier}$ of the chalcogen element-terminated V_2C

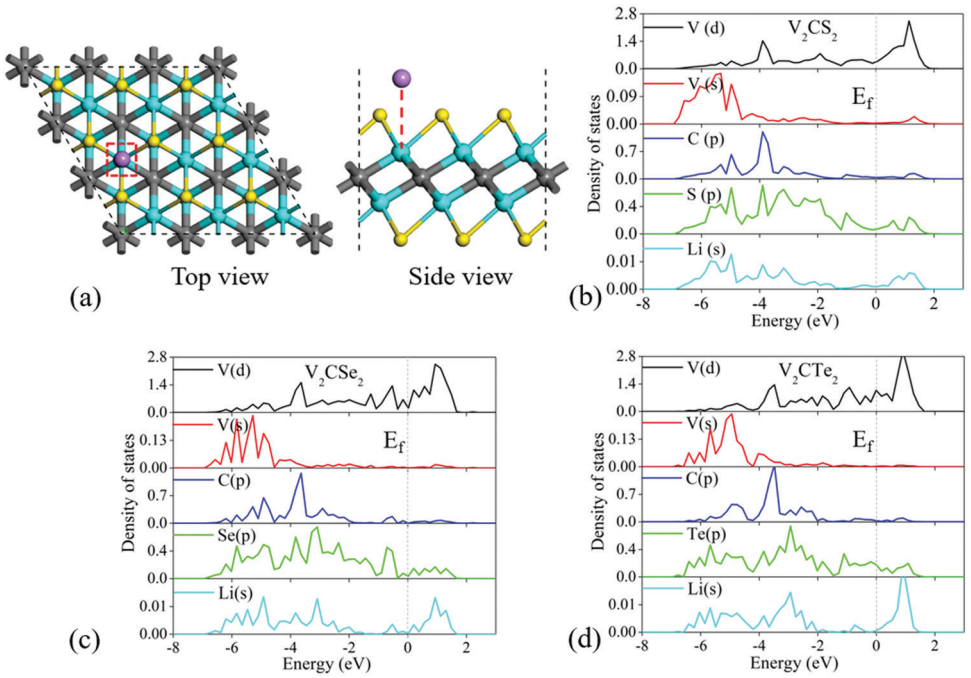

Fig. 3 (a) The structure of one Li-adsorbed V_2CX_2 at site A. The calculated partial density of states of one Li-adsorbed (b) monolayer V_2CS_2, (c) monolayer V_2CSe_2 and (d) monolayer V_2CTe_2, where the E_f is set to 0 eV.

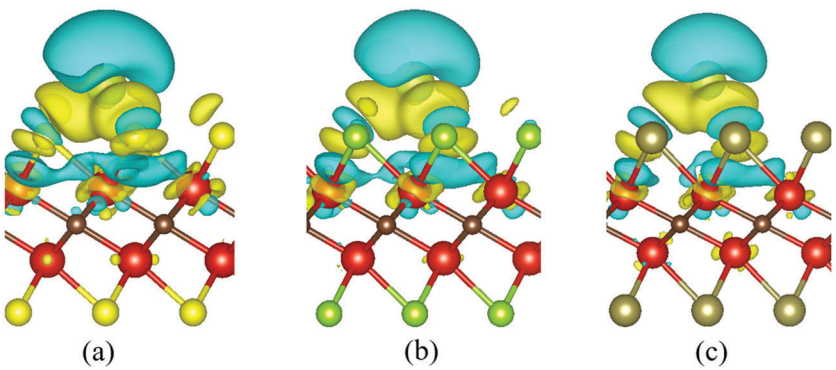

Fig. 4 The calculated difference charge densities of one Li-adsorbed (a) monolayer V_2CS_2, (b) monolayer V_2CSe_2 and (c) monolayer V_2CTe_2, with isosurface 0.008 e/borh^3; the blue region represents electron depletion, while the yellow region represents electron accumulation.

monolayer is lower than that of monolayer V_2CO_2 (0.30 eV). The higher $E_{barrier}$ of the Li atom on the monolayer V_2CO_2 compared with that on the V_2CS_2 monolayer is consistent with the previous research,[33] which means the faster migration of Li on the monolayer V_2CX_2 (X = S, Se, and Te) than that in the corresponding path on the monolayer V_2CO_2.

3.3 The Li storage capability of chalcogen terminated V_2CX_2 (X = S, Se, and Te)

In order to compare the Li capability of monolayer V_2CX_2, the E_{ad} values of the Li atoms on each layer are calculated using the following formula[30] to analyze the effect of chalcogen element on the Li capability:

$$E_{ad}(m) = (E_{V_2CX_2Li(m-1)} + 18E_{Li} - E_{V_2CX_2Lim})/18 \quad (9)$$

where $E_{ad}(m)$ is the E_{ad} of Li in the mth layer, and $E_{V_2CX_2Li_{18m}}$ is the total energy of monolayer V_2CX_2 with m Li layers on both sides. The energy per bcc-Li is calculated as 2.03 eV in this paper. Therefore, the E_{ad} can check the possibility of phase separation of the composite $V_2CX_2Li_m$.[61,62] The positive E_{ad} larger than the cohesive energy of bcc-Li indicates that the Li atoms can avoid the formation of dendrites and collapse of anode materials can be avoided. All Li atoms in the first layer are located on the most stable site A on the monolayer V_2CX_2. When putting a second layer of Li atoms in site C (*i.e.* beyond the chalcogen atoms) of the substrate, the total energy of the formed composite $V_2CX_2Li_4$ is the lowest for all X values. It can be known from Table 4 that monolayer V_2CS_2 can only adsorb one layer of Li atoms with the E_{ad} of 0.77 eV, which is consistent with previous research.[33] The E_{ad} (−0.04 eV) of the second layer

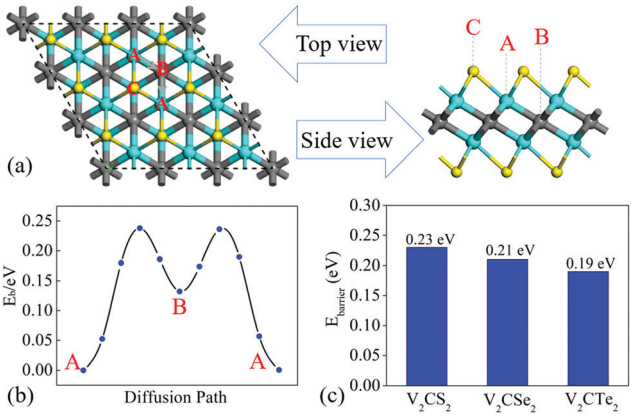

Fig. 5 (a)Top view of three adsorption sites and the most favorable diffusion path upon the monolayer V_2CS_2. (b) Energy profile of the A → B → A path upon monolayer V_2CS_2. (c) Column plots of $E_{barrier}$ from A → B for V_2CX_2 (X = S, Se, and Te).

Table 4 The E_{ad}, the area A, and the VER for the 3 × 3 super cell of monolayer V_2CX_2(X = S, Se, and Te)

	E_{ad} (eV)	A (Å)	VER (%)
$V_2CS_2Li_2$	0.77	9.68	11.6
$V_2CSe_2Li_2$	0.39	9.83	10.5
$V_2CSe_2Li_4$	0.02	9.63	6.1
$V_2CTe_2Li_2$	0.07	10.01	6.3
$V_2CTe_2Li_4$	0.04	9.92	4.4

Li atoms in the V_2CS_2 substrate becomes negative. The V_2CSe_2 and V_2CTe_2 monolayers can both adsorb two layers of Li atoms with the adoptable E_{ad}. The E_{ad} of the first Li layer on site A on both sides of monolayer V_2CSe_2 is 0.39 eV, and the E_{ad} of second Li layer on site C is 0.02 eV. The E_{ad} of first Li layer on site A in each side of monolayer V_2CTe_2 is 0.07 eV, and the E_{ad} of second Li layer on site C is 0.04 eV. When monolayers V_2CSe_2 and V_2CTe_2 adsorb more Li layers, the E_{ad} becomes negative, indicating that the clustering of Li atoms will happen.[61] The E_{ad} of the second Li layer on the monolayers V_2CSe_2 and V_2CTe_2 is comparable with that on monolayer Mo_2C(0.01 eV),[63] monolayer Nb_2C(0.02 eV)[64] and monolayer MoC_2(0.04 eV).[65] As shown in Table 5, according to Bader charge[58] analysis, when adsorbing second Li layer atoms, the charge transfer from one Li atom in the second layer to monolayer V_2CS_2, monolayer V_2CSe_2 and monolayer V_2CTe_2 is 0.29 e, 0.78 e and 0.79 e, respectively, which is consistent with their E_{ad}s (−0.04 eV, 0.02 eV and 0.04 eV) of second layer Li atoms and the same as that in the previous research about zirconium carbide MXene.[66] When comparing the data shown in Tables 5 and 3, it can be found that the charge transfer mainly happens between Li and chalcogen atoms, while the charges of other elements in the substrate rarely change during the lithiation process. Meanwhile, the maximum theoretical Li capacities (mA h g^{-1}) are calculated using the following formula:[67]

$$C = n\nu F10^3/M \quad (10)$$

where, M is the atomic mass of monolayer V_2CX_2, n is the number of adsorbed Li atoms, ν is the valency of the Li atom, and F is the Faraday constant (26.801 A h mol^{-1}).[67] Obviously, the calculated Li capacity of monolayer V_2CS_2 (301.08 mA h g^{-1}) is the same as that in previous research.[33] The Li capacities of monolayers V_2CSe_2 and V_2CTe_2 are 394.41 mA h g^{-1} and 290.45 mA h g^{-1}, respectively. Importantly, monolayer V_2CSe_2 can adsorb two Li layer atoms, thus resulting in the highest capacity, which is larger than that of graphite (372 mA h g^{-1}) (Table 6).[68]

Large VER will damage the cycle life of LIBs in practical applications. The lattice constants of the unit cell of three structures are 3.05 Å, 3.12 Å and 3.24 Å after the full lattice optimization, respectively. The VERs of the fully lithiated monolayer V_2CX_2(X = S, Se, and Te) shown in Table 4 are much lower than that of graphite (12%)[69] and far smaller than those of other ultrahigh capacity anodes such as germanium(370%),[70] Si(323%)[71] and Ti_n(259%).[72] They are also much smaller than those of the experimental critical values for the standards (<25%) for most LIB anodes.[73,74] Therefore, the VER of monolayer V_2CX_2 is rather ideal and it should be adoptable for the LIB anodes. In addition, the VERs of three structures are decreasing with the increased mass of chalcogen elements.

Finally, the AIMD simulation of monolayer $V_2CSe_2Li_4$ in the 3 × 3 super cell is performed, as shown in Fig. 6. The free energy fluctuates around a constant during the 5 ps total time at 300 K with the 1 fs time step. The structure remains intact without any apparent distortion, indicating its excellent thermodynamic stabilities. The $E_{barrier}$, Li capacity and VER show that monolayer V_2CSe_2 should be more feasible for LIB anodes than monolayer V_2CS_2.

The open circuit voltage (OCV) is an important quantity for the LIB anode materials. Commonly, the OCV for anodes should be positive and low to get a maximum capacity for the battery cell.[75] The OCV of monolayer $V_2CX_2Li_m$ can be estimated by the following formula:[76]

Table 5 The Bader charges of Li(Q_{Li}), C(Q_C), and V(Q_V) and X(Q_X) for the 3 × 3 super cell of the monolayer V_2CX_2(X = S, Se, and Te) with 36 Li atoms (two layers)

	V_2CS_2	V_2CSe_2	V_2CTe_2
V	1.269	1.191	1.087
C	−1.490	−1.152	−1.548
X	−1.152	−0.973	−0.802
Li (1st layer)	0.337	−0.240	−0.300
Li (2nd layer)	0.291	0.780	0.789

Table 6 The lattice constants, area and VER of the 3 × 3 super cell of the monolayer V_2CX_2(X = S, Se, and Te)

3 × 3 supercell	a (Å)	b (Å)	Area (Å^2)	VER (%)
V_2CS_2	9.16	9.16	72.59	—
$V_2CS_2Li_2$	9.68	9.68	81.15	12
$V_2CS_2Li_4$	9.55	9.55	78.98	8.8

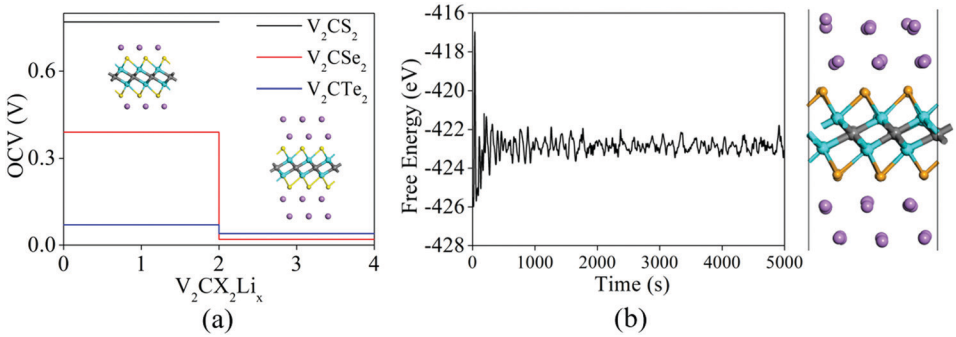

Fig. 6 (a) The OCVs of monolayer V_2CX_2 (X = S, Se, and Te) during lithiation when all composites are fully optimized. (b) The curve of free energy within 5 ps at 300 K with time step of 1 fs of lithiated $V_2CSe_2Li_4$ (left) and the snapshot after 5 ps (right).

$$\mathrm{OCV} = (E_{\mathrm{V_2CX_2Li_{(m-1)}}} + 18E_{\mathrm{Li}} - E_{\mathrm{V_2CX_2Li_m}})/18e \qquad (11)$$

The positive OCV ensures that the adsorption of Li atoms on the anode material is feasible, which can prevent the formation of metallic states.[77] The OCVs of monolayer V_2CX_2 plotted in Fig. 6(a) are positive. Obviously, the OCV of $V_2CSe_2Li_x$ ranges from 0.38 V to 0.02 V. Therefore, monolayer V_2CSe_2 has relatively low average OCV (0.2 V *vs.* Li/Li^+), indicating that it is suitable for serving as the anode materials.[14] Obviously, the average OCV of monolayer V_2CSe_2 of 0.2 V is comparable with that of monolayer W_2C (0.27 V).[78] Thus, monolayer V_2CSe_2 has high Li capacity, low E_{barrier} for the Li^+ ion, and small OCV when compared with those of graphite and other anode materials and should be the most ideal LIB anode material.

3.4 Chalcogen-terminated monolayer Ti_2CX_2 (X = S, Se, and Te)

In order to check whether the above results apply to other MXenes, we investigated the case of monolayer Ti_2CX_2 (X = S, Se, and Te). The previous research[79] has shown that the phonon spectrum of monolayer Ti_2CS_2 has no imaginary frequency and the AIMD demonstrates the thermodynamic stability of monolayer Ti_2CS_2. As shown in Fig. 7(a and b), the phonon spectra of Ti_2CSe_2 and Ti_2CTe_2 monolayers also have no imaginary frequency, indicating the dynamical stability of the Ti_2CSe_2 and Ti_2CTe_2 substrates. In addition, the AIMD is calculated to check the thermodynamic stabilities of monolayer Ti_2CSe_2 and monolayer Ti_2CTe_2. After 5 ps, the structure remains intact without apparent distortion when the temperature is set as 300 K and the time step is set as 1 fs. The free energy fluctuates around a constant value, as shown in Fig. 7(c and d). Thus, monolayer Ti_2CSe_2 and monolayer Ti_2CTe_2 show high thermodynamic stabilities.

We next calculate the Li storage capacity of monolayer Ti_2CX_2 (X = S, Se, and Te). However, monolayer Ti_2CX_2 (X = S, Se, and Te) can only store one Li layer on each side of the substrate, which is different from the case of monolayer V_2CX_2

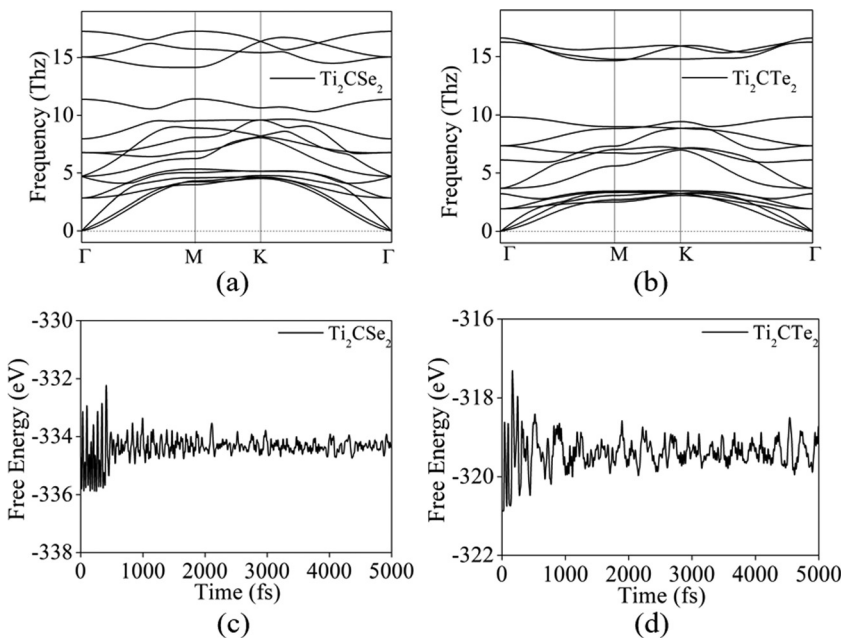

Fig. 7 The phonon spectra of the (a) monolayer Ti_2CSe_2 and (b) monolayer Ti_2CTe_2. The free energy variations of (c) monolayer Ti_2CSe_2 and (d) monolayer Ti_2CTe_2 within 5 ps during the AIMD simulation at 300 K.

(X = S, Se, and Te), with the E_{ad}s of 1.5 eV, 0.78 eV and 0.26 eV, respectively. The corresponding Li storage capacities are 311.84 mA h g^{-1}, 208.83 mA h g^{-1} and 147.68 mA h g^{-1} for monolayer Ti_2CX_2 (X = S, Se, and Te). Amongst all, monolayer Ti_2CSe_2 adsorbs only one Li layer on each side and has low Li storage capacity when compared with that of monolayer V_2CSe_2.

4. Conclusion

The metallic properties of monolayer V_2CX_2 (X = S, Se, and Te) can ensure fast electron transport in the charge/discharge process when used as the LIB anode. The dynamical stabilities are verified by the phonon spectra. The thermodynamic stabilities are verified by AIMD simulation. The E_{ad} and $E_{barrier}$ of V_2CX_2 (X = S, Se, and Te) decrease with the increasing atomic number of the terminated element. Monolayer V_2CSe_2 shows higher Li capacity (394.41 mA h g^{-1}), relatively low $E_{barrier}$ (0.21 eV) and small VER(6.1%) when compared with that of monolayer V_2CX_2 (X = O, S, and Te). Thus, monolayer V_2CSe_2 has high Li capacity, low $E_{barrier}$ for the Li^+ ion, and small OCV when compared with graphite and other anode materials and should be the most ideal LIB anode material. Monolayer V_2CS_2 can adsorb one-layer Li atoms and then achieve the Li capacity of 301.08 mA h g^{-1}, while monolayer V_2CTe_2 can adsorb multi-layer Li atoms and then achieve the Li capacity of 290.45 mA h g^{-1}. The composite $V_2CX_2Li_n$ shows high thermodynamic stability during the AIMD at 300 K after 5 ps, which is consistent with its small VER. These excellent properties indicate that monolayer chalcogen-terminated V_2C has promising applications as a LIB anode.

Conflicts of interest

There are no conflicts to declare.

Acknowledgements

This work is financially sponsored by the Fundamental Research Funds for the Central Universities (Grant No. B200202001), the Natural Science Foundation of Jiangsu Province (Grant No. BK20161501), the Postgraduate Research & Practice Innovation Program of Jiangsu Province (Grant No. KYCX18_0521), Six talent peaks project in Jiangsu Province (Grant No. 2015-XCL-010), and the Open Subject of National Laboratory of Solid State Microstructures (Grant No. M32055).

References

1 A. Manthiram, X. Yu and S. Wang, Lithium battery chemistries enabled by solid-state electrolytes, *Nat. Rev. Mater.*, 2017, **2**(4), 16103.
2 W. J. Zhang, A review of the electrochemical performance of alloy anodes for lithium-ion batteries, *J. Power Sources*, 2011, **196**(1), 13–24.
3 H. Wu and Y. Cui, Designing nanostructured Si anodes for high energy lithium ion batteries, *Nano Today*, 2012, **7**(5), 414–429.
4 A. L. M. Reddy, A. Srivastava, S. R. Gowda, H. Gullapalli, M. Dubey and P. M. Ajayan, Synthesis of nitrogen-doped graphene films for lithium battery application, *ACS Nano*, 2010, **4**(11), 6337–6342.
5 C. Huang, S. Zhang, H. Liu, Y. Li, G. Cui and Y. Li, Graphdiyne for high capacity and long-life lithium storage, *Nano Energy*, 2015, **11**, 481–489.
6 L. Zhou, S. Yan, L. Pan, X. Wang, Y. Wang and Y. Shi, A scalable sulfuration of WS 2 to improve cyclability and capability of lithium-ion batteries, *Nano Res.*, 2016, **9**(3), 857–865.
7 K. R. G. Lim, A. D. Handoko, S. K. Nemani, B. Wyatt, H. Y. Jiang, J. Tang, B. Anasori and Z. W. Seh, Rational design of two-dimensional transition metal carbide/nitride (MXene) hybrids and nanocomposites for catalytic energy storage and conversion, *ACS Nano*, 2020, **14**(9), 10834–10864.
8 M. Naguib, J. Halim, J. Lu, K. M. Cook, L. Hultman, Y. Gogotsi and M. W. Barsoum, New two-dimensional niobium and vanadium carbides as promising materials for Li-ion batteries, *J. Am. Chem. Soc.*, 2013, **135**(43), 15966–15969.
9 F. Liu, J. Zhou, S. Wang, B. Wang, C. Shen, L. Wang, Q. Hu, Q. Huang and A. Zhou, Preparation of high-purity V2C MXene and electrochemical properties as Li-ion batteries, *J. Electrochem. Soc.*, 2017, **164**(4), A709–A713.
10 J. Halim, S. Kota, M. R. Lukatskaya, M. Naguib, M. Q. Zhao, E. J. Moon, J. Pitock, J. Nanda, S. J. May, Y. Gogotsi and M. W. Barsoum, Synthesis and characterization of 2D molybdenum carbide (MXene), *Adv. Funct. Mater.*, 2016, **26**(18), 3118–3127.
11 A. D. Handoko, S. N. Steinmann and Z. W. Seh, Theory-guided materials design: two-dimensional MXenes in electro-and photocatalysis, *Nanoscale Horiz.*, 2019, **4**(4), 809–827.
12 J. Zhu, A. Chroneos, J. Eppinger and U. Schwingenschlögl, S-functionalized MXene as electrode materials for Li-ion batteries, *Appl. Mater. Today*, 2016, **5**, 19–24.
13 Y. Lee, S. B. Cho and Y. C. Chung, Tunable indirect to direct band gap transition of monolayer Sc_2CO_2 by the strain effect, *ACS Appl. Mater. Interfaces*, 2014, **6**(16), 14724–14728.
14 Q. Meng, A. Hu, C. Zhi and J. Fan, Theoretical prediction of MXene-like structured Ti_3C_4 as a high capacity electrode material for Na ion batteries, *Phys. Chem. Chem. Phys.*, 2017, **19**(43), 29106–29113.
15 L. Bai, H. Yin and X. Zhang, Energy storage performance of $V_{n+1}C_n$ monolayer as electrode material studied by first-principles calculations, *RSC Adv.*, 2016, **6**(60), 54999–55006.
16 Y. Zhou and X. Zu, Mn_2C sheet as an electrode material for lithium-ion battery: A first-principles prediction, *Electrochim. Acta*, 2017, **235**, 167–174.
17 S. Zhao, X. Meng, K. Zhu, F. Du, G. Chen, Y. Wei, Y. Gogotsi and Y. Gao, Li-ion uptake and increase in interlayer spacing of Nb_4C_3 MXene, *Energy Storage Mater.*, 2017, **8**, 42–48.

18 V. Shukla, N. K. Jena, S. R. Naqvi, W. Luo and R. Ahuja, Modelling high-performing batteries with MXenes: The case of S-functionalized two-dimensional nitride MXene electrode, *Nano Energy*, 2019, **58**, 877–885.
19 F. Liu, A. Zhou, J. Chen, H. Zhang, J. Cao, L. Wang and Q. Hu, Preparation and methane adsorption of two-dimensional carbide Ti_2C, *Adsorption*, 2016, **22**(7), 915–922.
20 M. H. Tran, T. Schäfer, A. Shahraei, M. Dürrschnabel, L. Molina-Luna, U. I. Kramm and C. S. Birkel, Adding a new member to the MXene family: synthesis, structure, and electrocatalytic activity for the hydrogen evolution reaction of $V_4C_3T_x$, *ACS Appl. Energy Mater.*, 2018, **1**(8), 3908–3914.
21 M. Ghidiu, J. Halim, S. Kota, D. Bish, Y. Gogotsi and M. W. Barsoum, Ion-exchange and cation solvation reactions in Ti_3C_2 MXene, *Chem. Mater.*, 2016, **28**(10), 3507–3514.
22 O. Mashtalir, M. R. Lukatskaya, M. Q. Zhao, M. W. Barsoum and Y. Gogotsi, Amine-assisted delamination of Nb_2C MXene for Li-ion energy storage devices, *Adv. Mater.*, 2015, **27**(23), 3501–3506.
23 K. D. Fredrickson, B. Anasori, Z. W. Seh, Y. Gogotsi and A. Vojvodic, Effects of applied potential and water intercalation on the surface chemistry of Ti2C and Mo_2C MXenes, *J. Phys. Chem. C*, 2016, **120**(50), 28432–28440.
24 X. Liang, A. Garsuch and L. F. Nazar, Sulfur cathodes based on conductive MXene nanosheets for high-performance lithium–sulfur batteries, *Angew. Chem.*, 2015, **127**(13), 3979–3983.
25 J. Zhu, A. Chroneos, J. Eppinger and U. Schwingenschlögl, S-functionalized MXene as electrode materials for Li-ion batteries, *Appl. Mater. Today*, 2016, **5**, 19–24.
26 Q. Meng, J. Ma, Y. Zhang, Z. Li, C. Zhi, A. Hu and J. Fan, The S-functionalized Ti_3C_2 MXene as a high capacity electrode material for Na-ion batteries: a DFT study, *Nanoscale*, 2018, **10**(7), 3385–3392.
27 V. Shukla, N. K. Jena, S. R. Naqvi, W. Luo and R. Ahuja, Modelling high-performing batteries with MXene: The case of S-functionalized two-dimensional nitride MXene electrode, *Nano Energy*, 2019, **58**, 877–885.
28 M. Lu, H. Li, W. Han, J. Chen, W. Shi, J. Wang, X. M. Meng, J. Qi, H. Li, B. Zhang, W. Zhang and W. Zheng, 2D titanium carbide (MXene) electrodes with lower-F surface for high performance lithium-ion batteries, *J. Energy Chem.*, 2019, **31**, 148–153.
29 M. Wu, B. Wang, Q. Hu, L. Wang and A. Zhou, The Synthesis Process and Thermal Stability of V_2C MXene, *Materials*, 2018, **11**(11), 2112.
30 J. Hu, B. Xu, C. Ouyang, S. A. Yang and Y. Yao, Investigations on V2C and V_2CX_2(X = F, OH) monolayer as a promising anode material for Li ion batteries from first-principles calculations, *J. Phys. Chem. C*, 2014, **118**(42), 24274–24281.
31 D. Sun, Q. Hu, J. Chen, X. Zhang, L. Wang, Q. Wu and A. Zhou, Structural transformation of MXene (V_2C, Cr_2C, and Ta_2C) with O groups during lithiation: a first-principles investigation, *ACS Appl. Mater. Interfaces*, 2015, **8**(1), 74–81.
32 Y. Xie, M. Naguib, V. N. Mochalin, M. W. Barsoum, Y. Gogotsi, X. Yu, K. W. Nam, X. Q. Yang, A. I. Kolesnikov and P. R. C. Kent, Role of surface structure on Li-ion energy storage capacity of two-dimensional transition-metal carbides, *J. Am. Chem. Soc.*, 2014, **136**(17), 6385–6394.
33 Y. M. Li, Y. L. Guo and Z. Y. Jiao, The effect of S-functionalized and vacancies on V_2C MXenes as anode materials for Na-ion and Li-ion batteries, *Curr. Appl. Phys.*, 2020, **20**(2), 310–319.
34 B. Yan, C. Lu, P. Zhang, J. Chen, W. He, W. Tian, W. Zhang and Z. Sun, Oxygen/sulfur decorated 2D MXene V2C for promising lithium ion battery anodes, *Mater. Today Commun.*, 2020, **22**, 100713.
35 Y. Wang, J. Shen, L. C. Xu, Z. Yang, R. Li, R. Liu and X. Li, Sulfur-functionalized vanadium carbide MXene (V_2CS_2) as a promising anchoring material for lithium–sulfur batteries, *Phys. Chem. Chem. Phys.*, 2019, **21**(34), 18559–18568.
36 V. Kamysbayev, A. S. Filatov, H. Hu, X. Rui, F. Lagunas, D. Wang, R. F. Klie and D. V. Talapin, Covalent surface modifications and superconductivity of two-dimensional metal carbide MXenes, *Science*, 2020, **369**(6506), 979–983.
37 K. R. G. Lim, A. D. Handoko, L. R. Johnson, X. Meng, M. Lin, G. S. Subramanian, B. Anasori, Y. Gogotsi, A. Vojvodic and Z. W. Seh, 2H-MoS2 on Mo_2CT_x MXene Nanohybrid for Efficient and Durable Electrocatalytic Hydrogen Evolution, *ACS Nano*, 2020, **14**(11), 16140–16155.
38 G. Kresse and D. Joubert, From ultrasoft pseudopotentials to the projector augmented-wave method, *Phys. Rev. B: Condens. Matter Mater. Phys.*, 1999, **59**(3), 1758.
39 P. E. Blöchl, Projector augmented-wave method, *Phys. Rev. B: Condens. Matter Mater. Phys.*, 1994, **50**(24), 17953.
40 G. Kresse and J. Furthmüller, Efficient iterative schemes for ab initio total-energy calculations using a plane-wave basis set, *Phys. Rev. B: Condens. Matter Mater. Phys.*, 1996, **54**(16), 11169.
41 J. P. Perdew, J. A. Chevary, S. H. Vosko, K. A. Jackson, M. R. Pederson, D. J. Singh and C. Fiolhais, Atoms, molecules, solids, and surfaces: Applications of the generalized gradient approximation for exchange and correlation, *Phys. Rev. B: Condens. Matter Mater. Phys.*, 1992, **46**(11), 6671.
42 J. P. Perdew, K. Burke and M. Ernzerhof, Generalized gradient approximation made simple, *Phys. Rev. Lett.*, 1996, **77**(18), 3865.
43 S. Grimme, Semiempirical GGA-type density functional constructed with a long-range dispersion correction, *J. Comput. Chem.*, 2006, **27**(15), 1787–1799.
44 K. Parlinski, Z. Q. Li and Y. Kawazoe, First-principles determination of the soft mode in cubic ZrO_2, *Phys. Rev. Lett.*, 1997, **78**(21), 4063.
45 G. Henkelman, B. P. Uberuaga and H. Jónsson, A climbing image nudged elastic band method for finding saddle points and minimum energy paths, *J. Chem. Phys.*, 2000, **113**(22), 9901–9904.
46 G. Henkelman and H. Jónsson, Improved tangent estimate in the nudged elastic band method for finding minimum energy paths and saddle points, *J. Chem. Phys.*, 2000, **113**(22), 9978–9985.
47 S. Nosé, A unified formulation of the constant temperature molecular dynamics methods, *J. Chem. Phys.*, 1984, **81**(1), 511–519.

48 S. Nose, Molecular dynamics simulations, *Prog. Theor. Phys.*, 1991, **103**, 1–117.
49 D. M. Bylander and L. Kleinman, Energy fluctuations induced by the Nosé thermostat, *Phys. Rev. B: Condens. Matter Mater. Phys.*, 1992, **46**(21), 13756.
50 X. Ji, K. Xu, C. Chen, B. Zhang, H. Wan, Y. Ruan, L. Miao and J. Jiang, Different charge-storage mechanisms in disulfide vanadium and vanadium carbide monolayer, *J. Mater. Chem. A*, 2015, **3**(18), 9909–9914.
51 L. Feng, X. H. Zha, K. Luo, Q. Huang, J. He, Y. Liu, W. Deng and S. Du, Structures and mechanical and electronic properties of the Ti_2CO_2 MXene incorporated with neighboring elements (Sc, V, B and N), *J. Electron. Mater.*, 2017, **46**(4), 2460–2466.
52 H. Zabel, Phonons in layered compounds, *J. Phys.: Condens. Matter*, 2001, **13**(34), 7679.
53 M. Born and K. Huang, *Dynamical theory of crystal lattices*, Clarendon press, 1954.
54 J. Wang, S. Yip, S. R. Phillpot and D. Wolf, Crystal instabilities at finite strain, *Phys. Rev. Lett.*, 1993, **71**(25), 4182.
55 K. H. Michel and B. Verberck, Theory of elastic and piezoelectric effects in two-dimensional hexagonal boron nitride, *Phys. Rev. B: Condens. Matter Mater. Phys.*, 2009, **80**(22), 224301.
56 T. Zhao, S. Zhang, Y. Guo and Q. Wang, TiC_2:a new two-dimensional sheet beyond MXene, *Nanoscale*, 2016, **8**(1), 233–242.
57 R. C. Andrew, R. E. Mapasha, A. M. Ukpong and N. Chetty, Mechanical properties of graphene and boronitrene, *Phys. Rev. B: Condens. Matter Mater. Phys.*, 2012, **85**(12), 125428.
58 G. Henkelman, A. Arnaldsson and H. Jónsson, A fast and robust algorithm for Bader decomposition of charge density, *Comput. Mater. Sci.*, 2006, **36**(3), 354–360.
59 B. Zhang, L. Fan, J. Hu, J. Gu, B. Wang and Q. Zhang, MnB_2 nanosheet and nanotube: stability, electronic structures, novel functionalization and application for Li-ion batteries, *Nanoscale*, 2019, **11**(16), 7857–7865.
60 S. T. Oyama, D. Lee, P. Hacarlioglu and R. F. Saraf, Theory of hydrogen permeability in nonporous silica membranes, *J. Membr. Sci.*, 2004, **244**(1-2), 45–53.
61 E. Lee and K. A. Persson, Li absorption and intercalation in single layer graphene and few layer graphene by first principles, *Nano Lett.*, 2012, **12**(9), 4624–4628.
62 X. Fan, W. T. Zheng, J. L. Kuo and D. J. Singh, Adsorption of single Li and the formation of small Li clusters on graphene for the anode of lithium-ion batteries, *ACS Appl. Mater. Interfaces*, 2013, **5**(16), 7793–7797.
63 Q. Sun, Y. Dai, Y. Ma, T. Jing, W. Wei and B. Huang, Ab initio prediction and characterization of Mo_2C monolayer as anodes for lithium-ion and sodium-ion batteries, *J. Phys. Chem. Lett.*, 2016, **7**(6), 937–943.
64 J. Hu, B. Xu, C. Ouyang, Y. Zhang and S. A. Yang, Investigations on Nb 2 C monolayer as promising anode material for Li or non-Li ion batteries from first-principles calculations, *RSC Adv.*, 2016, **6**(33), 27467–27474.
65 Y. Yu, Z. Guo, Q. Peng, J. Zhou and Z. Sun, Novel two-dimensional molybdenum carbides as high capacity anodes for lithium/sodium-ion batteries, *J. Mater. Chem. A*, 2019, **7**(19), 12145–12153.
66 Q. Meng, J. Ma, Y. Zhang, Z. Li, A. Hu, J. J. Kai and J. Fan, Theoretical investigation of zirconium carbide MXene as prospective high capacity anode materials for Na-ion batteries, *J. Mater. Chem. A*, 2018, **6**(28), 13652–13660.
67 D. Datta, J. Li and V. B. Shenoy, Defective graphene as a high-capacity anode material for Na-and Ca-ion batteries, *ACS Appl. Mater. Interfaces*, 2014, **6**(3), 1788–1795.
68 M. Broussely and G. Archdale, Li-ion batteries and portable power source prospects for the next 5-10 years, *J. Power Sources*, 2004, **136**(2), 386–394.
69 K. Persson, Y. Hinuma, Y. S. Meng, A. Van der Ven and G. Ceder, Thermodynamic and kinetic properties of the Li-graphite system from first-principles calculations, *Phys. Rev. B: Condens. Matter Mater. Phys.*, 2010, **82**(12), 125416.
70 C. K. Chan, X. F. Zhang and Y. Cui, High capacity Li ion battery anodes using Ge nanowires, *Nano Lett.*, 2008, **8**(1), 307–309.
71 J. C. Arrebola, A. Caballero, J. L. Gómez-Cámer, L. Hernán, J. Morales and L. Sánchez, Combining 5 V $LiNi_{0.5}Mn_{1.5}O_4$ spinel and Si nanoparticles for advanced Li-ion batteries, *Electrochem. Commun.*, 2009, **11**(5), 1061–1064.
72 P. Meduri, C. Pendyala, V. Kumar, G. U. Sumanasekera and M. K. Sunkara, Hybrid tin oxide nanowires as stable and high capacity anodes for Li-ion batteries, *Nano Lett.*, 2009, **9**(2), 612–616.
73 S. Zhao, W. Kang and J. Xue, The potential application of phosphorene as an anode material in Li-ion batteries, *J. Mater. Chem. A*, 2014, **2**(44), 19046–19052.
74 V. V. Kulish, O. I. Malyi, C. Persson and P. Wu, Phosphorene as an anode material for Na-ion batteries: a first-principles study, *Phys. Chem. Chem. Phys.*, 2015, **17**(21), 13921–13928.
75 D. Das, R. P. Hardikar, S. S. Han, K. R. Lee and A. K. Singh, Monolayer BC_2: an ultrahigh capacity anode material for Li ion batteries, *Phys. Chem. Chem. Phys.*, 2017, **19**(35), 24230–24239.
76 K. T. Chan, J. B. Neaton and M. L. Cohen, First-principles study of metal adatom adsorption on graphene, *Phys. Rev. B: Condens. Matter Mater. Phys.*, 2008, **77**(23), 235430.
77 Q. Zhang, J. Ma, M. Lei and R. Quhe, Metallic MoN layer and its application as anode for lithium-ion batteries, *Nanotechnology*, 2018, **29**(16), 165402.
78 V. Shukla, N. K. Jena, S. R. Naqvi, W. Luo and R. Ahuja, Modelling high-performing batteries with Mxenes: The case of S-functionalized two-dimensional nitride Mxene electrode, *Nano Energy*, 2019, **58**, 877–885.
79 X. Liu, X. Shao, F. Li and M. Zhao, Anchoring effects of S-terminated Ti_2C MXene for lithium-sulfur batteries: A first-principles study, *Appl. Surf. Sci.*, 2018, **455**, 522–526.